Reduced-Order Model for Viscous Aerodynamic Flow Past an Airfoil

D. Alonso,* J. M. Vega,† and A. Velazquez‡
Universidad Politecnica de Madrid, 28040 Madrid, Spain

A method is presented to obtain reduced-order models of multiparametric, steady, transonic aerodynamic flows around two-dimensional airfoils. The method is based on proper orthogonal decomposition and appropriate projection on the proper orthogonal decomposition manifold of the governing equations and boundary conditions, and it includes various ingredients that are new in this field. Proper orthogonal decomposition modes are obtained from a set of snapshots calculated by computational fluid dynamics based on the compressible Navier–Stokes equations and a turbulence model, but projection on the proper orthogonal decomposition manifold is made using the inviscid Euler equations, which makes the method independent of the computational fluid dynamics scheme; projection is made using only a limited number of mesh points, obtaining quite good results. Shock waves are treated specifically in the proper orthogonal decomposition description, to avoid the need of using a too-large number of snapshots. The method is checked and discussed on a specific aerodynamic problem.

Nomenclature

A_i	=	ith amplitude of the smooth field
B_i	=	ith amplitude of the trace of the shock wave
BC_i	=	ith boundary condition
C_i	=	ith amplitude of the internal shape of the shock wave
C_p	=	pressure coefficient
C'_{p0}	=	threshold of the x derivative pressure coefficient for shock wave existence
D_j	=	distance of the jth snapshot to the approximated test case
EQ_i	=	ith Euler equation in conservative form
eq_i	=	ith Euler equation in differential form
F	=	safety factor
H	=	fitness function
L_1	=	half-width of the shock wave interval
L_2	=	half-width of the interval in which the genetic algorithm is allowed to search the minimum
L_3	=	half-width of the interval in which the mass flux vector is smoothed
M	=	Mach number
N	=	number of modes used for a given test point and region
N_0	=	maximum number of snapshots
N_1	=	twice the initial estimate of the proper orthogonal decomposition manifold dimension
$\tilde{N}_1$	=	number of modes taken after the first proper orthogonal decomposition
N_2	=	product of F by $\tilde{N}_1$
n	=	coordinate along the lines perpendicular to the airfoil
n_x, n_z	=	horizontal and vertical components of the outward unit normal vector to the contour Γ
P_i	=	ith mode of the pressure
p	=	pressure
Q_j	=	generic jth mode of the state variable
q_j	=	generic jth state variable
R_i	=	ith mode of the density
R_{ij}	=	elements of the covariance matrix
s	=	coordinate along the lines parallel to the airfoil
s_{crit}	=	the minimum s value of upstream limit of the shock wave intervals
s_{limit}	=	point where $\rho w/(\rho u) = 1$
s_{sw}^{wall}	=	position of the shock wave on the airfoil
T_i	=	ith mode of the trace
t_{sw}	=	trace of the shock wave
U_i	=	ith mode of the horizontal velocity field
u	=	horizontal velocity component
W_i	=	ith mode of the vertical velocity field
w	=	vertical velocity component
x, z	=	horizontal and vertical coordinates
α_{kl}	=	lth element of the kth eigenvector of the covariance matrix R
Γ	=	boundary of the domain Ω
γ	=	specific heat ratio (nondimensional)
Δ	=	jump of a variable
ε	=	upper bound of the error
λ_i	=	ith eigenvalue of the covariance matrix
μ	=	scaling factor for the internal-shape covariance matrix
ρ	=	density
σ_k	=	kth singular value of the covariance matrix R
τ	=	scaling factor for the conservative Euler equations
φ	=	sigmoidal function
Ω	=	domain

Subscripts

BC	=	upstream region where the boundary conditions are imposed
ref	=	reference value

Superscripts

CFF	=	complete flowfield
IS	=	internal shape
MIS	=	modified internal shape
PS	=	pressure side
SF	=	smooth field
SS	=	suction side
t	=	trace of the shock wave

*Postdoctoral Researcher, Aerospace Propulsion and Fluid Mechanics Department, School of Aeronautics, Plaza del Cardenal Cisneros 3; diego.alonso.fernandez@upm.es.
†Professor, Applied Mathematics Department, School of Aeronautics, Plaza del Cardenal Cisneros 3; josemanuel.vega@upm.es.
‡Associate Professor, Aerospace Propulsion and Fluid Mechanics Department, School of Aeronautics, Plaza del Cardenal Cisneros 3; angel.velazquez@upm.es.

I. Introduction

CONCEPTUAL design is a very important step in the design process of aeronautic products. In practice, it involves a compromise between cost and time, because of the need to explore a wide spectrum of possible solutions. Accordingly, it is important to develop tools that are both fast and accurate, because of the implications that their use has downstream in the design flowchart. In this frame, reduced-order models (ROMs) may provide a complementary option to explore wider portions of a given parameter space at an affordable cost. Computational fluid dynamics (CFD) calculations are still needed, of course, because they provide the information (snapshots) required to generating the modal expansions that are to be used in the ROM; however, their number can be kept to a minimum and, henceforth, cost as well.

The search for stable and robust ROMs in various contexts, not restricted to aerodynamics, is a trend that can be easily traced in the specialized literature. Very recently, Barone et al. [1] have reported on a Galerkin projection procedure for compressible flow modeling that emphasizes algorithm stability. An interesting conclusion of this paper is that the selection of the inner product for the projection plays an important role in the scheme stability. Regarding the formulation of the modal expansions, the authors explicitly state in their introduction that "it is still desirable to be able to generate a stable ROM regardless of the quality of the POD basis used to generate it." Stability of the ROM also depends on the size of the chosen basis, as shown in the paper by Bui-Thanh et al. [2]. In particular, the authors point out that the selection of an appropriate set of snapshots still remains an open issue if the usual inner product is used, even though balanced POD [3,4] and weighted scalar product [5] methods reduce the number of required snapshots using appropriate inner products. Some methods to derive computationally efficient ROMs for nonlinear problems have been considered, either through appropriate interpolation of nonlinear terms [6] or by assuming a functional form of these [7]. Further simplification of the physics model of a ROM formulation, in the frame of acoustic loading applications for aircraft structures, has been addressed by Hollkamp and Gordon [8]. In this work, the authors did not explicitly account for membrane displacements in their ROM, but condensed them into the nonlinear stiffness terms of the bending equations. This displacement was recovered a posteriori using a set of estimated membrane displacement basis. In a different framework, but related to the issue of algorithm robustness, the stability of the ROM of some electric circuits has been studied by Bai et al. [9].

Regarding now the specific issue of the application of ROMs to problems of interest in the aerospace sector, it is important to mention the work of LeGresley and Alonso [10], who developed a ROM for inviscid subsonic aerodynamic flows around 2-D airfoils. Lieu et al. [11] addressed the development of a fluid–structure ROM for a complete F-16 fighter aircraft configuration at Mach numbers in the range from 0.61 to 1.15. Also in the field of transonic aeroelasticity, Iemma and Gennaretti [12] have developed a ROM-based methodology that can be applied to 3-D wings. This work is based on the hypothesis that unsteady transonic flow can be approximated by the superposition of a nonlinear mean steady flow and a linear unsteady small perturbation. Thomas et al. [13] have presented a method to improve the performance of some ROMs formulations used to predict, among other cases of interest, flutter for the AGARD 445.6 wing. In the same technical area, Allen et al. [14] have worked in the development of control laws, based on ROMs, to suppress flutter with the objective of increasing the extent of the aircraft flight envelope. Finally, a comprehensive review on the types and use of ROMs, mainly for aerospace applications, has been provided by Lucia et al. [15].

An intriguing question about ROM formulation (not often addressed in the literature) is whether the ROM itself must to be based on the same set of equations used in CFD calculations. In principle, the answer should be yes. However, it is to be noted that the CFD snapshots used to generate the modes already contain information derived from the original equations. Thus, it may be worth exploring the possibility of using a ROM based on simpler

equations, to obtain a ROM that is more robust and independent of CFD details. In other words, model reduction could be achieved in two complementary steps:

1) The flow variables are modeled via POD modal expansions based on snapshots obtained using CFD with the complete equations.

2) The ROM is derived by projecting flow equations that are simpler than the original ones in modal expansions.

Step 2 cannot be generalized, because its validity is most likely dependent on the type of problem under consideration. In particular, in this paper we explore the possibility of developing a ROM for compressible airfoil flow based on the Euler equations, while the original problem is turbulent, and the CFD snapshots have been computed using the Navier–Stokes equations with a turbulence model and, possibly, some small stabilizing terms added for numerical reasons. This approach is supported a priori by three related arguments:

1) Viscous effects in a high Reynolds number flow are confined to thin and well-localized regions (boundary layers, shear layers, and shock waves), and thus contributions of the neglected viscous and stabilizing terms on the integral projected terms [see Eqs. (9) and (10)] are small.

2) The required vorticity distribution information needed to reconstruct the correct solutions (which cannot be completely calculated using Euler equations) is already present in the POD modes.

3) The actual physics of the problem does not depend on the turbulence model and the stabilizing terms used in CFD; the latter are only numerical artifacts.

In our opinion, the development of a ROM based on the Euler equations when the original snapshots are turbulent exhibits some advantages that could be of interest for practical industrial applications:

1) The snapshots used to generate the modal expansions could be computed using various turbulence models. In this sense, the method presented in the following sections is independent of the flow solvers and the turbulence models considered for the snapshots generation.

2) The ROM itself does not need artificial numerical terms to stabilize the convergence process. Furthermore, even if the CFD flow solver requires artificial viscosity terms to stabilize the algorithm (which is most likely) the ROM does not mimic these terms. Thus, it produces what we could call a *clean* solution.

3) The ROM gains numerical robustness. The reason is that this simplified formulation allows for the use of a minimization strategy to find its solution that is robust itself [16,17], because it does not require the use of higher order flow derivatives.

In addition to the use of the Euler equations to derive the ROMs (which is new in the literature, to our knowledge), two ingredients are convenient to further improve computational efficiency. These are also new (except for our previous work in [17,18]) and are related with shock waves and the number of mesh points required in ROM calculations.

An important issue in deriving ROMs able to deal with transonic flows is connected with the presence of shock waves that move significantly as the parameters are varied. As further explained in [18], if moving shock waves are present, then either the resulting POD modes are stairlike-shaped (instead of exhibiting the correct one-jump, shock wave shape), which yields a poor approximation, or both the number of required snapshots and the dimension of the POD manifold are very large.

This is because POD approximations are made up of linear combinations, and linear combinations of shifted jumps do not yield jumps, but stairs; see Fig. 1, where a CFD solution is compared with interpolated approximations using POD based on snapshots that contain shock waves. Note that a single pressure jump is substituted in the method by three unphysical jumps. Thus, it is clear that a specific shock wave treatment is necessary to obtain ROMs in transonic conditions at a reasonable computational cost. In this paper, such a treatment will be the natural extension of that presented in [18], which only applies to the pressure distribution on the airfoil surface, and must be combined here with projection of the governing equations on the POD manifold.
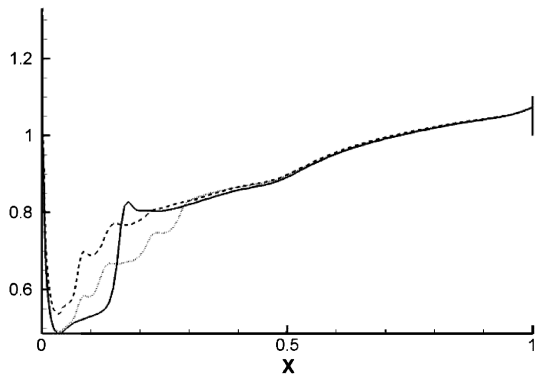
Fig. 1   POD reconstruction over the wall in the suction side without any shock wave treatment at test point PT24 (see Table 1) using the POD plus interpolation (dashed line) and plain interpolation with neighboring snapshots (dotted line), as compared with CFD (solid line).

A third simplification in ROMs calculation results from the observation (already made and checked in [17]) that determining the POD-mode amplitudes should require information from a number of mesh points that is much smaller than that required in the CFD solution; see also [6] for a related approach that selects mesh points based on empirical interpolation. In fact, if all calculations were exact, information from a number of points equal to the number of unknown amplitudes would be enough. Since calculations are not exact, this number should be larger than the number of POD modes. It will also be convenient that the points being selected contain as much information as feasible about the flow and are as free as possible of CFD errors. In some sense, the underlying idea is the same as that behind the method of snapshots [10,19]. Let us mention here that this third simplification opens up new possibilities that make our method quite flexible. For example, considering only a region of the flowfield where none of the snapshots exhibits shock waves, we shall be able to calculate the POD approximation with great accuracy in this region (see Secs. III.B.2 and III.B.5). Discarding regions with largest CFD errors will also provide better results.

The main object of this paper is to improve the method described in [17] to make it appropriate to deal with shock wave structures; in addition, the feasibility of using the Euler equations in a limited number of mesh points to calculate the POD-mode amplitudes, will be checked. These require revising the basic concepts of reduced-order modeling, seeking as much flexibility as possible, which will lead to further improvements of the method. Even though the method applies to general aerodynamic problems, for the sake of clarity the main ideas are explained using a specific test problem, which is described in Sec. II. The method itself is developed in Sec. III and results are presented and discussed in Sec. IV. The paper ends with some concluding remarks in Sec. V.

II.   Test Problem Description

We consider the aerodynamic flow around an airfoil, plotted in Fig. 2a. This is a research airfoil that is used by the research and development industrial community to check shock wave detection methods; the x and z scales are not given because of confidentiality reasons. CFD snapshots are calculated using the TAU code [20,21], which is a finite volume discretization of the compressible continuity, momentum, and energy equations, with viscous terms modified according to an Edwards-corrected Spalart–Allmaras turbulence model [22] and some small stabilizing terms added for numerical reasons. The complete computational mesh, shown in Fig. 2b, contains 55,578 points and consists of two parts, an O-shaped structured mesh around the airfoil (with 20,458 points) and an outer unstructured mesh. The boundary of the domain, accounting for the far field, is located 50 chords away from the airfoil. Some discretization errors are present near the common boundary of both meshes, which (as usually happens with industrial CFD codes using qualitatively different meshes) result from abrupt jumps in the mesh topology. These errors are dealt with below, ignoring the outer five
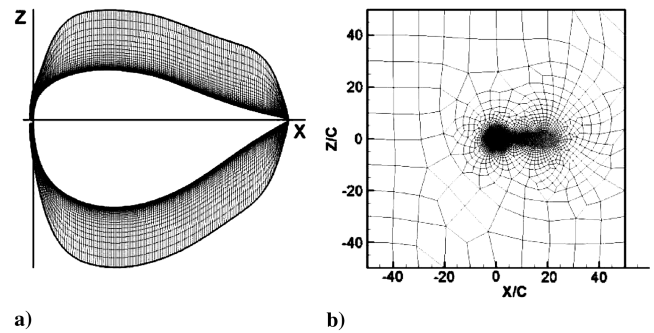

Fig. 2   CFD mesh: a) O-mesh and b) complete mesh.

lines of the structured O-mesh in the definition of the various residuals that will be minimized [e.g., those defined in Eqs. (12) and (13)]. Note that this is possible, because of the possibility of using a projection window to define the residuals, instead of the whole computational mesh, which is one of the main outcomes of the paper.

The parameter space is a rectangle in the AOA–M (angle of attack vs Mach number) plane, in the range $-3° < \text{AOA} < 3°$ and $0.4 < M < 0.8$. Note that such a parameter range includes transonic flows with strong shock waves, either in the pressure or suction sides; shock waves in both sides are also present in some cases. Still, the shock wave position varies significantly (up to one-third of the chord) as the parameters are varied.

As anticipated above, the Euler equations will be used to obtain the POD-mode amplitudes. Instead of the original flow variables (namely, density, pressure, temperature, and velocity components), we shall eliminate the temperature using the equation of state and use as new variables the density, the pressure, and the mass fluxes in the x and z directions, which are nondimensionalized using their values (labeled with the subscript BC) in the far upstream region (called the BC region), where the inlet boundary conditions are imposed. The reference values for nondimensionalization are

$$\rho_{\text{ref}} = \rho_{\text{BC}}, \qquad p_{\text{ref}} = p_{\text{BC}},$$
$$\rho u_{\text{ref}} = \rho w_{\text{ref}} = \frac{\sqrt{(\rho u)_{\text{BC}}^2 + (\rho w)_{\text{BC}}^2}}{M}$$

Thus, the dimensionless density and pressure in the BC region are both equal to one, but the dimensionless mass fluxes in this region are $(\rho u, \rho w)_{\text{BC}} = M(\cos \text{AOA}, \sin \text{AOA})$.

As anticipated above, the ROM can be derived using only a part of the computational mesh. Here, we consider only the O-shaped curvilinear structured mesh around the airfoil (see Fig. 2a), which facilitates derivation of the ROM and improves computational efficiency. For convenience, we shall work independently on the pressure and suction sides of the airfoil, which are limited by the leading-edge point (defined as that point where the tangent to the airfoil is orthogonal to the freestream velocity at zero incidence) and the trailing-edge point. We shall use two curvilinear coordinates s and n, along lines parallel to the airfoil and perpendicular to it, respectively, (Fig. 3). The origin of the Cartesian coordinate system, (x, z), is at the leading-edge point; the x axis also passes through the trailing edge and the z axis is perpendicular to the x axis and points toward the suction side.

III.   Method Description

For the sake of clarity, a brief description of the method is first given in seven steps.

1) A set of N_0 solutions (called snapshots) is calculated using CFD, which provides scalar fields in each flow variable.

2) Some of the snapshots exhibit shock waves. These are treated identifying a shock wave region and decomposing the associated complete flowfield (CFF) in each flow variable into two parts: namely, a smooth field (SF) and a shock wave field (SWF). The SWF contains the spatial jumps in the flow variables that make POD decomposition not appropriate. These jumps are absent in the SF, and
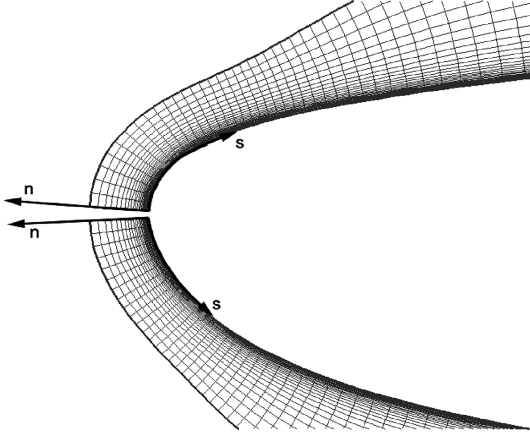
Fig. 3   New coordinate system.

thus POD decomposition is effective with this field. The SWFs in turn are decomposed into four basic structures that are themselves amenable to POD treatment. These basic structures are the following ones: the position of the shock wave on the airfoil's surface (s_{sw}^{wall}); the curve that describes the shock wave position inside the flowfield as it separates from the wall, which will be called the trace of the shock wave (t_{sw}); the jumps of the flow variables across the shock wave [$\Delta(\rho u)$, $\Delta(\rho w)$, $\Delta\rho$, and Δp]; and the internal shape (IS) of the shock wave, which is defined by the local distribution of the flow variables [$(\rho u)^{IS}$, $(\rho w)^{IS}$, ρ^{IS}, and p^{IS}]. Both the shock wave position and the trace are common to all flow variables, but the jump and the internal shape must be calculated independently for each flow variable. The shock wave treatment is explained in Sec. III.A.

3) Then the POD modes associated with the CFF, the SF, and the various shock wave structures are calculated. As further explained in Sec. III.B, this will be done as follows:

　　a) Consider appropriate subregions in the spatial O-mesh (instead of the complete O-mesh) and a limited number of mesh points.

　　b) Consider a subset of the complete set of snapshots. That set will depend on the particular parameter values for which the solution is being sought, which will make POD decomposition much more effective.

4) A first guess of the POD-mode amplitudes is calculated using POD plus interpolation in the parameter space, as developed in [18] and recalled in Sec. III.B.5.

5) The POD-mode amplitudes of the CFF are calculated minimizing a properly defined residual (see Sec. III.C.1). Again, the residual will involve only a small number of mesh points in the O-mesh and can be defined in two ways, either:

　　a) Add (for the selected mesh points) the square roots of the absolute values of the left-hand sides of the governing Euler equations and boundary conditions, as we did in [17]. This requires good approximations on the derivatives of the flow variables, which will need some preprocessing.

　　b) Write down the governing equations in conservative form and integrate them in some smooth subregions of the O-mesh. These integrals are transformed into line integrals on the boundaries of the subregions using the divergence theorem; the resulting residual is obtained upon adding the square roots of the absolute values of the line integrals and boundary conditions. Since no spatial derivatives are needed, preprocessing is not performed in this case.

6) Compare the CFF obtained in the last step with its counterpart for the SF, provides the jumps of the flow variables across the shock wave. The amplitudes of the remaining shock wave structures are calculated in Sec. III.C.2 using a discretized version of the Rankine–Hugoniot conditions (see, e.g., [23]).

7) Repeat steps 5 and 6 iteratively until the approximation is converged.

The various minimization processes described above are performed using a genetic algorithm (GA), which selects the POD-mode amplitudes as the minimizers of the residuals. Such a method will be called proper orthogonal decomposition plus genetic algorithm (POD plus GA) hereafter. Of course, gradientlike methods such as steepest-descent based on Broyden-like approximations [24] could be used to obtained much faster ROMs, but robustness of the GA is quite appropriate in the context of this paper. By robustness, we mean here that the GA somewhat looks for minimizers in a wide window in the parameter space. Robustness of the GA itself in connection with the GA parameters will be ensured by selecting these by calibration.

A.　Shock Wave Treatment

As already anticipated above, snapshots that exhibit steep jumps that move along the airfoil as the parameters are varied are decomposed into various flow structures, which are considered now.

1.　Identification of the Shock Wave: Shock Wave Position and Trace

For each coordinate line n = constant, we first calculate the pressure coefficient, defined as

$$C_p = 2\frac{p-1}{\gamma M^2}$$

in terms of the specific heat ratio γ, and evaluate the x derivative of C_p. If there is at least one point that verifies the inequality

$$\frac{\partial C_p}{\partial x} > C'_{p0}$$

where C'_{p0} is a threshold value whose selection requires some calibration ($C'_{p0} = 9$ is a good selection for the test problem considered below), this particular snapshot is assumed to exhibit a shock wave, provided that the point where the x derivative of C_p is largest [which defines the streamwise shock wave position at each wall-normal stage, $s_{sw}(n)$] is located not too close to the leading edge; a distance from the leading edge larger than 1.5% of the airfoil chord is a good selection in the test problem below. Such a condition excludes steep gradients caused by the strong suction peak near the leading edge, and need not be treated, since they do not move as the parameters are varied. The selection of the threshold value $C'_{p0} = 9$ and the 1.5% distance to the leading edge could be varied (to, e.g., 8 and 1.3%, respectively) without significant effects on the results. These calibration parameters of the method have been chosen examining the snapshots, which showed that in the considered parameter range:

1) All shock waves exhibit a central region where the x derivatives of the flow variables are largest and correlated among each other, which means that a criteria based on the x derivative of C_p is reasonable.

2) The size of the suction peak near the leading edge is small and fairly constant. Using these observations, the threshold values mentioned above are easily selected.

It must be noted that the calibration above depends on the parameter range. In other words, the calibration should be revisited if a different parameter range were considered. For instance, the stagnation point is sensitive to the angle of attack and the 1.5% distance selected above should be increased if the interval from -3 to $3°$ in the angle of attack were enlarged.

As defined above, the values of $s_{sw}(n)$ are necessarily integer numbers. This means that the function $s_{sw} = s_{sw}(n)$ is stairlike-shaped, which is not appropriate for POD-mode decomposition. Thus, such a function is smoothed out using a convolution, defined as

$$s_{sw}^{conv}(1) = s_{sw}(1), \qquad s_{sw}^{conv}(2) = \tfrac{1}{4}(s_{sw}(1) + 2s_{sw}(2) + s_{sw}(3))$$

$$s_{sw}^{conv}(i) = \tfrac{1}{9}(s_{sw}(i-2) + 2s_{sw}(i-1) + 3s_{sw}(i) + 2s_{sw}(i+1)$$

$$+ s_{sw}(i+2)) \quad \text{if } 2 < i < h-1$$

$$s_{sw}^{conv}(h-1) = \tfrac{1}{4}(s_{sw}(h-2) + 2s_{sw}(h-1)$$

$$+ s_{sw}(h)), s_{sw}^{conv}(h) = s_{sw}(h) \tag{1}$$

where h is the total number of points of the Cartesian mesh in the n direction. Such a convolution is applied twice. The smoothing effect of convolution is illustrated in Fig. 4.

Once the shock wave has been located in each coordinate line, the shock wave position on the airfoil and the trace $t_{sw}(n)$ are defined as

$$s_{sw}^{wall} = s_{sw}^{conv}(1), \qquad t_{sw}(n) = s_{sw}^{conv}(n) - s_{sw}^{wall}$$

To obtain an initial guess of the possible shock wave structures at points of the parameter space where existence of shock wave is dubious, we must also define a position over the wall and a trace for snapshots that do not exhibit true shock waves. These false position and trace are defined as those of the nearest snapshot in the parameter space that exhibits a shock wave.

2. Shock Wave Interval and Jump, the Smooth Field, and Shock Wave Field

For each coordinate line $n = $ constant, we define the shock wave interval as

$$[s_{sw}^{wall} + t_{sw}(n) - L_1 + 1, s_{sw}^{wall} + t_{sw}(n) + L_1]$$

in terms of the half-width L_1, which has been selected as $L_1 = 6$ in the test problem below. Again, this calibration has been made as above, examining the available snapshots, noting that the width of the shock waves if fairly constant, independently of the associated values of the parameters M and AOA. This is understandable, since such a width only depends on a balance between convective and diffusive terms. Using this, selection of the threshold value L_1 readily follows. For each flowfield variable, the jump of the variable is defined as the total jump across the shock wave interval. The SF is defined along each line $n = $ constant, 1) as equal to the CFF upstream of the shock wave region, 2) as constant in the shock wave interval, and 3) as equal to the CFF minus the shock wave jump downstream of the shock wave interval. Thus, we have a continuous field that may exhibit jumps in the spatial derivative, which are smoothed out applying twice the same convolution already applied to the trace [see Eq. (1)]. To preserve the original snapshots, the SWF is obtained by subtracting the SF from the CFF. Figure 5 shows the decomposition of the CFF into the SF and SWF. As can be seen, the method provides smooth s derivatives everywhere (including the vicinity of the shock wave); the (untreated) n derivatives have proved to be smooth too.

Finally, the IS is defined as the SWF scaled with the jump and referred to a new s coordinate, $\tilde{s}$, obtained from the original one by a shift that locates the origin at the center of the shock wave interval: namely, $\tilde{s} = s - s_{sw}^{wall} - t_{sw}(n)$. Note that the IS varies from zero to 1 in.the shock wave interval; it also retains the unphysical overshooting effect (seemingly, an artifact of stabilization terms in
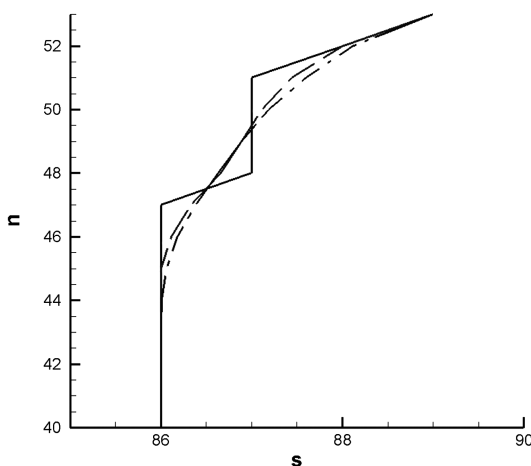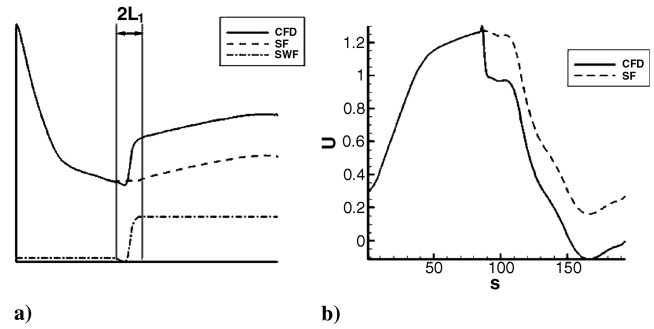

Fig. 5 Plots of a) new division of the original snapshots into the SF and the SWF and b) original CFD calculation and its corresponding SF.

the CFD numerical code), which is sometimes found near the shock wave and makes the internal shape not completely smooth.

This process must be applied to the four flow variables and to all snapshots, including those that do not verify the criterion for shock wave existence, given above. For the latter snapshots, the jump and the internal shape cannot be calculated as above; instead, the jump of the variables is set to zero and the internal shape is imposed to be the sigmoidal function:

$$\varphi(s) = \frac{1}{1 + e^{-\xi(s)}} \tag{2}$$

where the function $\xi(s)$ has been calibrated as

$$\xi(s) = 7 + \frac{14}{2 \cdot L_1 - 1}(s - s_{sw}^{wall} - t_{sw}(n) - L_1)$$

At this stage, we have defined the shock wave position, the trace, the jump, the internal shape, and the smooth field, which are functions of the type

$$s_{sw}^{wall} = s_{sw}^{wall}(\text{AOA}, M), t_{sw} = t_{sw}(\text{AOA}, M, n),$$

$$\Delta(\rho u, \rho w, \rho, p) = \Delta(\rho u, \rho w, \rho, p)(\text{AOA}, M, n),$$

$$(\rho u, \rho w, \rho, p)^{IS} = (\rho u, \rho w, \rho, p)^{IS}(\text{AOA}, M, s, n),$$

$$(\rho u, \rho w, \rho, p)^{SF} = (\rho u, \rho w, \rho, p)^{SF}(\text{AOA}, M, s, n)$$

B. POD Modes for the Smooth Field and the Various Shock Wave Structures

We first recall POD, and then apply it to the various flowfield components.

1. POD Methodology

Given N_0 snapshots (namely, vectors on a state variable that may correspond either to a flow variable distribution associated with smooth field or to the trace of the shock wave), $q_1, \ldots, q_{N_0}$, the associated POD modes are denoted as $Q_1, \ldots, Q_{N_0}$ and can be written as

$$Q_k = \frac{1}{\sigma_k} \sum_{l=1}^{N_0} \alpha_{kl} q_l$$

where α_{kl} and σ_k are calculated through the eigenvectors and eigenvalues of the covariance matrix R: namely,

$$\sum_{l=1}^{N_0} R_{kl} \alpha_{ml} = (\sigma_m)^2 \alpha_{mk}$$

The latter is defined as $R_{kl} = \langle q_k, q_l \rangle$, where $\langle, \rangle$ is an appropriate inner product that will be defined below. The square roots of the associated eigenvalues of R, $\sigma_1, \ldots, \sigma_{N_0}$, are called *singular values* of the snapshots matrix. Invoking well-known POD formulas, the number of retained modes N can now be selected as the minimum integer, such that

Fig. 4 Position of the shock wave $s_{sw}(n)$ as a function of the coordinate n in the case AOA $= -3.0°$, $M = 0.8$: without convolution (solid line), with a convolution applied once (dashed), and with a convolution applied twice (dotted-dashed).

$$\sqrt{\sum_{i=N+1}^{N_0} \sigma_i^2 \bigg/ \sum_{i=1}^{N_0} \sigma_i^2} < \varepsilon_0 \qquad (3)$$

for some predetermined root-mean-square-error (RMSE) bound ε_0. Errors are defined here using the norm $\|q\| = \sqrt{\langle q, q \rangle}$ After truncation, we expand the state variable (associated below either with the smooth field, the internal shape, or the trace) in terms of its retained modes, as

$$q = \sum_{k=1}^{N} A_k Q_k$$

2. POD Modes for the Smooth Field and the Complete Field

A computationally efficient treatment of the CFF and the SF requires some care. This is because these two structures exhibit a more complex topology than the trace and the internal shape.

Let us now consider the complete flowfield, CFF, whose POD treatment must be made using points in the O-mesh outside the region affected by the shock waves (to avoid spurious stairlike structures, as anticipated in Sec. I). To make the region affected by the shock waves as small as possible, we treat the pressure and suction sides independently and define the POD manifold locally in the parameter space. The O-mesh is first divided into two overlapping regions, shown in Fig. 6. Each region includes the whole part of the O-mesh we intend to describe (either the suction or the pressure side) plus that subregion in the opposite side bounded by the cross section of the O-mesh at $s = s_{\mathrm{crit}}$, where s_{crit} is the minimum (among the whole set of N_0 snapshots) of the upstream limit of the shock wave intervals defined in Sec. III.A.2. POD modes (and amplitudes) of the CFF are defined independently for each of these two regions. In addition, we still decompose each of these two regions into three subregions (see Figs. 6 and 7): namely, a *leading-edge region* (LER), defined as $-s_{\mathrm{crit}} < s < s_{\mathrm{sw}}^{\mathrm{wall}} - L_2$, a *shock wave region* (SWR), defined as $s_{\mathrm{sw}}^{\mathrm{wall}} - L_2 \leq s \leq s_{\mathrm{sw}}^{\mathrm{wall}} + L_2$, and a *trailing-edge region* (TER), defined as $s > s_{\mathrm{sw}}^{\mathrm{wall}} - L_2$. Here, $s_{\mathrm{sw}}^{\mathrm{wall}}$ is an estimate of the shock wave position and L_2 is defined such that the shock wave position is in the interval $s_{\mathrm{sw}}^{\mathrm{wall}} - L_2 \leq s \leq s_{\mathrm{sw}}^{\mathrm{wall}} + L_2$; these two quantities must be recalibrated in each GA run.

To decrease both the size of the region SWR and the number of required POD modes, we do not use all available snapshots, which would provide a unique POD manifold for all values of the parameters. Instead, a smaller set of snapshots is selected (with a method described in Appendix A) that depends on the particular values of the parameters and provides a smaller POD manifold. In other words, the POD manifold is defined locally in the parameter space.

Once the snapshots have been selected, the POD modes of the complete flowfield are calculated from the covariance matrix

$$R_{ij}^{\mathrm{CFF}} = \langle (\rho u, \rho, p)_i^{\mathrm{CFF}}, (\rho u, \rho, p)_j^{\mathrm{CFF}} \rangle$$

where the inner product $\langle , \rangle$ is defined as (recall that we are using the dimensionless flow variables)

$$\langle (\rho u, \rho, p)_1, (\rho u, \rho, p)_2 \rangle$$
$$= \frac{1}{\int_\Omega \mathrm{d}A} \int_\Omega (\rho_1 u_1 \rho_2 u_2 + \rho_1 \rho_2 + p_1 p_2) \, \mathrm{d}A \qquad (4)$$
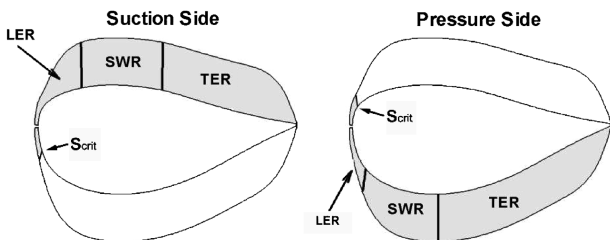

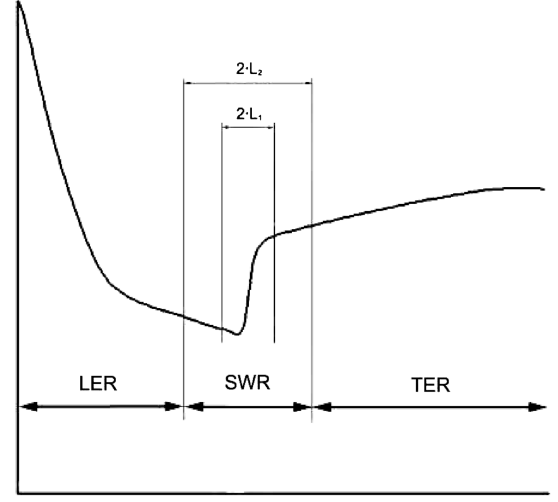**Fig. 6 Regions used to calculate the POD manifold of the smooth field.**

Fig. 7   Sketch of the subregions in which the airfoil is divided in both the pressure and suction sides.

Here, the integration domain is one of the two overlapping regions, shown in Fig. 6, depending on whether we are treating the pressure or the suction side. The resulting POD modes allow us to write the flow variables as

$$\begin{pmatrix} (\rho u)^{\mathrm{CFF}} \\ (\rho w)^{\mathrm{CFF}} \\ \rho^{\mathrm{CFF}} \\ p^{\mathrm{CFF}} \end{pmatrix} = \sum_i A_i(\mathrm{AOA}, M) \begin{pmatrix} U_i^{\mathrm{CFF}}(s, n) \\ W_i^{\mathrm{CFF}}(s, n) \\ R_i^{\mathrm{CFF}}(s, n) \\ P_i^{\mathrm{CFF}}(s, n) \end{pmatrix} \qquad (5)$$

where A_i denotes the POD-mode amplitudes, which are common to the four flow variables. These expansions well approximate the CFF in both the LER and TER, but not in the SWR, which does not matter, because the approximation (5) will only be used in the former two regions. In fact, we now take advantage of the fact that, by definition, the CFF and the SF exactly coincide in the LER defined above. Thus, we define modes on the smooth flowfield, $U_i^{\mathrm{SF}}, W_i^{\mathrm{SF}}, R_i^{\mathrm{SF}}$, and P_i^{SF} as those combinations of the original snapshots such that $U_i^{\mathrm{SF}} = U_i^{\mathrm{CFF}}$, $W_i^{\mathrm{SF}} = W_i^{\mathrm{CFF}}$, $R_i^{\mathrm{SF}} = R_i^{\mathrm{CFF}}$, and $P_i^{\mathrm{SF}} = P_i^{\mathrm{CFF}}$ in the leading-edge region. This is done writing down the SF modes as linear combinations of the original snapshots with the same coefficients that appear when the CFF modes are written in terms of the snapshots associated with the smooth fields. Thus, since both the snapshots and the POD modes of both the complete fields and the smooth fields exactly coincide in the LER, the POD amplitudes of the CFF must coincide with those of the SF: namely,

$$\begin{pmatrix} (\rho u)^{\mathrm{SF}} \\ (\rho w)^{\mathrm{SF}} \\ \rho^{\mathrm{SF}} \\ p^{\mathrm{SF}} \end{pmatrix} = \sum_i A_i(\mathrm{AOA}, M) \begin{pmatrix} U_i^{\mathrm{SF}}(s, n) \\ W_i^{\mathrm{SF}}(s, n) \\ R_i^{\mathrm{SF}}(s, n) \\ P_i^{\mathrm{SF}}(s, n) \end{pmatrix} \qquad (6)$$

And the difference between the SF and the CFF in the TER provides the jump across the shock wave, which allows for calculating the latter without any additional treatment.

Now the resulting POD modes on both the CFF and the SF could lead to large errors in the spatial derivatives (even in the LER and the TER, where no shock wave is expected) of the wall-normal velocity component (perpendicular to the airfoil), which is significantly smaller than the tangential component. This is because the CFD code is based on finite volume discretization, while the derivatives are naturally calculated using finite differences. To avoid such errors, the POD modes of the CFF can be postprocessed using the continuity equation, as explained in Appendix B. Such postprocessing will only be done when spatial derivatives are needed, as described below.

3. POD Modes for the Trace and the Internal Shape

POD treatment of the trace and the internal shape is standard and performed considering all available snapshots, even those that exhibit false shock waves.

As explained above, the trace of the shock wave is a function of the parameters and the wall-normal coordinate n. Isolating dependence on n, POD modes T_i are calculated in terms of the snapshots t_{sw} using the covariance matrix:

$$R^t_{ij} = \langle t_{swi}, t_{swj} \rangle \equiv \frac{1}{h} \sum_{n=1}^{h} t_{swi}(n) t_{swj}(n)$$

This inner product can also be used to evaluate distances between different traces. The trace is expanded in POD modes, as

$$t_{sw}(\text{AOA}, M, n) = \sum_i B_i(\text{AOA}, M) T_i(n) \qquad (7)$$

where the POD-mode amplitudes B_i will be calculated below.

Concerning the internal shape of the shock wave, it is first decomposed into two parts, as

$$(\rho u, \rho w, \rho, p)_i^{\text{IS}} = (\rho u, \rho w, \rho, p)_i^{\text{MIS}} + \frac{\tilde{s} - 1 + L_1}{2L_1 - 1}(1,1,1,1)$$

where the first term in the right-hand side will be called modified internal shape (MIS) below, and the second term is such that the MIS vanishes at the extreme values of the shock wave interval (namely, $\tilde{s} = 1 - L_1$ and $\tilde{s} = L_1$). Thus, the MIS is appropriate to apply POD. The MIS depends on the parameters and the curvilinear coordinates. Isolating dependence on s and n, POD modes are defined using the covariance matrix:

$$R_{ij}^{\text{MIS}} = \langle (\rho u, \rho w, \rho, p)_i^{\text{MIS}}, (\rho u, \rho w, \rho, p)_j^{\text{MIS}} \rangle$$

$$\equiv \mu \sum_{s=1}^{2L_1} \sum_{n=1}^{h} [(\rho u)_i^{\text{MIS}}(s,n)(\rho u)_j^{\text{MIS}}(s,n)$$

$$+ (\rho w)_i^{\text{MIS}}(s,n)(\rho w)_j^{\text{MIS}}(s,n)]$$

$$+ \mu \sum_{s=1}^{2L_1} \sum_{n=1}^{h} [\rho_i^{\text{MIS}}(s,n)\rho_j^{\text{MIS}}(s,n) + p_i^{\text{MIS}}(s,n)p_j^{\text{MIS}}(s,n)]$$

where the common scaling factor is defined as $\mu = (2 \cdot L_1 \cdot h)^{-1}$ and, as above, the inner product $\langle , \rangle$ can be used to evaluate distances between different internal shapes. Now the flow variables are written as expansions on the POD modes, U_i^{IS}, W_i^{IS}, R_i^{IS}, and P_i^{IS}, as

$$\begin{pmatrix} (\rho u)^{\text{IS}} \\ (\rho w)^{\text{IS}} \\ \rho^{\text{IS}} \\ p^{\text{IS}} \end{pmatrix} = \sum_{i=1}^{N} C_i(\text{AOA}, M) \begin{pmatrix} U_i^{\text{MIS}}(s,n) \\ W_i^{\text{MIS}}(s,n) \\ R_i^{\text{MIS}}(s,n) \\ P_i^{\text{MIS}}(s,n) \end{pmatrix}$$

$$+ \frac{\tilde{s} - 1 + L_1}{2L_1 - 1} \begin{pmatrix} 1 \\ 1 \\ 1 \\ 1 \end{pmatrix} \qquad (8)$$

where C_i are the POD-mode amplitudes, which are common to the four flow variables and will be calculated below.

4. Reconstruction of the CFF in the Complete O-Mesh

As defined above, the SF has been calculated independently in the overlapping suction and pressure regions (see Fig. 6). A joint representation of the SF in the whole O-mesh is obtained as

$$(\rho u)^{\text{SF}}(s,n) = \varphi(s)(\rho u)^{\text{PS}}(s,n) + (1 - \varphi(s))(\rho u)^{\text{SS}}(s,n),$$

$$(\rho w)^{\text{SF}}(s,n) = \varphi(s)(\rho w)^{\text{PS}}(s,n) + (1 - \varphi(s))(\rho w)^{\text{SS}}(s,n)$$

where the superscripts PS and SS stand for the pressure and suction sides, and φ is the sigmoidal function defined in Eq. (2), with the function $\xi(s)$ being a linear function that maps the overlapping s interval $-s_{\text{crit}} < s < s_{\text{crit}}$ into the interval $[-7, 7]$. The SWF is obtained by multiplying the IS by the jump and shifting the s coordinate to its original value, taking into account both the position of the shock wave on the airfoil and the trace. Finally, the CFF is obtained by adding the SF and SWF.

5. POD Plus Interpolation

To begin with, the expansions (5–8) defined above are truncated according to the condition (3). Proceeding as indicated in Sec. III.B.4, we can reconstruct any of the original snapshots, which provide the mode amplitudes at the associated parameter values. The mode amplitudes for other parameter values are interpolated using the Akima's bivariate interpolation method for scattered data [25]. Since both SVD/POD and interpolation are numerically inexpensive, the method only requires less than one-tenth of a CPU-second per mode in a standard desktop PC. The result of POD plus interpolation will be used as an initial guess in the residual minimization method that is considered next.

C. Minimization of the Residual Function

The unknown amplitudes A_i (two sets of amplitudes, for the regions in the pressure and suction sides), B_i, and C_i are calculated upon minimization of a properly defined residual implementing a GA, using the amplitude values obtained via POD plus interpolation as the initial guess, as explained in the last section.

The residual associated with the complete flowfields is calculated in terms of the dimensionless Euler equations, which will be considered below both in differential and conservative forms. The former is written as

$$\text{eq}_1 \equiv \frac{\partial(\rho u)}{\partial x} + \frac{\partial(\rho w)}{\partial z} = 0$$

$$\text{eq}_2 \equiv \frac{1}{\rho}\left(\rho u \frac{\partial(\rho u)}{\partial x} + \rho w \frac{\partial(\rho u)}{\partial z} + \beta \rho u\right) + \frac{1}{\gamma}\frac{\partial p}{\partial x} = 0$$

$$\text{eq}_3 \equiv \frac{1}{\rho}\left(\rho u \frac{\partial(\rho w)}{\partial x} + \rho w \frac{\partial(\rho w)}{\partial z} + \beta \rho w\right) + \frac{1}{\gamma}\frac{\partial p}{\partial z} = 0$$

$$\text{eq}_4 \equiv \rho u \frac{\partial p}{\partial x} + \rho w \frac{\partial p}{\partial z} + \gamma \beta p - \frac{p}{\rho}\left(\rho u \frac{\partial \rho}{\partial x} + \rho w \frac{\partial \rho}{\partial z}\right) = 0 \quad (9)$$

where the quantity β is given by

$$\beta = eq_1 - \frac{\rho u}{\rho}\frac{\partial \rho}{\partial x} - \frac{\rho w}{\rho}\frac{\partial \rho}{\partial z}$$

The conservative form of the Euler Eqs. (9) is obtained as usual: integrating in Ω and applying the divergence theorem, which yields

$$\text{EQ}_1 \equiv \tau \oint [\rho u n_x + \rho w n_z]\, \text{d}l = 0$$

$$\text{EQ}_2 \equiv \tau \oint \left[\left(\frac{\rho u \rho u}{\rho} + \frac{1}{\gamma}p\right)n_x + \left(\frac{\rho u \rho w}{\rho}\right)n_z\right] \text{d}l = 0$$

$$\text{EQ}_3 \equiv \tau \oint \left[\left(\frac{\rho u \rho w}{\rho}\right)n_x + \left(\frac{\rho w \rho w}{\rho} + \frac{1}{\gamma}p\right)n_z\right] \text{d}l = 0$$

$$\text{EQ}_4 \equiv \tau \oint [\delta(\rho u n_x + \rho w n_z)]\, \text{d}l = 0 \qquad (10)$$

where the line integrals are extended to the boundary of the domain Ω, l is the arc length along the boundary, and

$$\delta = \frac{1}{\rho^2}\left[\rho p + \frac{\gamma - 1}{2}(\rho u \rho u + \rho w \rho w)\right], \qquad \tau = \left(\oint \text{d}l\right)^{-1}$$

The contour integrals are applied over a set of closed curves that will be called *cycles* below and are approximated by the trapezoidal

rule. In particular, the conservative form of the equations will be used to calculate the shock wave structures, taking the domain Ω as an appropriate domain across the shock wave, similar to what is done to obtain the classical Rankine–Hugoniot conditions.

The freestream boundary conditions, which will also be needed below, are written as

$$BC_1 \equiv \rho u - M\rho \cos(\text{AOA}) = 0$$
$$BC_2 \equiv \rho w - M\rho \sin(\text{AOA}) = 0$$
$$BC_3 \equiv \rho - 1 = 0$$
$$BC_4 \equiv p - 1 = 0 \qquad (11)$$

After these preliminaries, we proceed to calculate the various POD-mode amplitudes defined in Sec. III.B.

1. Calculation of the CFF, the SF, and the Shock Wave Jump

We first calculate the POD-mode amplitudes in the expansion (6) of the CFF, A_i, minimizing a residual. As we did in [17], we can define the residual as

$$H = \sum_{k=1}^{N_E} \sum_{i=1}^{4} \sqrt{|\text{eq}_i(s_k, n_k)|} + \sum_{m=1}^{N_{BC}} \sum_{i=1}^{4} \sqrt{|\text{BC}_i(s_m, n_m)|} \qquad (12)$$

where eq_i and BC_i stand for the left-hand sides of the Eqs. (9) and boundary conditions (11). This residual involves spatial derivatives and thus needs the postprocessing of the snapshots described in Appendix B. To avoid the need of postprocessing, we can use the following residual, which does not involve spatial derivatives, because it is obtained by calculating the conservative Eqs. (10) for a family of spatial domains, $\Omega_1, \ldots, \Omega_{N_E}$:

$$H = \sum_{k=1}^{N_E} \sum_{i=1}^{4} \sqrt{|\text{EQ}_i(\Gamma_k)|} + \sum_{m=1}^{N_{BC}} \sum_{i=1}^{4} \sqrt{|\text{BC}_i(s_m, n_m)|} \qquad (13)$$

Here, EQ_i denotes the left-hand sides of the conservation Eqs. (10) and for each k, Γ_k is the boundary of the subdomain Ω_k. The residual (13) is closely related to that already used in [10].

As anticipated in Sec. I, the right-hand side of (12) is evaluated only at some points (s_k, n_k) and (s_m, n_m) of the O-mesh and the BC region, respectively. In particular, the selected points of the O-mesh are taken in the LER and TER (to avoid the shock wave regions), outside the boundary layer (to avoid viscous effects not accounted for in the Euler equations) and not too close to the upper boundary of the O-mesh (to avoid CFD errors). Similarly, the contour integrals in (13) are extended to a set of small domains scattered in the LER and the TER, with the same restrictions above. The number of selected points or contour integrals must be just somewhat larger than the number of POD modes (four times the number of POD modes are considered in the example below). The selected points or contour integrals are chosen equispaced in both directions, but can also be chosen randomly without losing precision in the results. In the n direction, we take four (this number has been calibrated) equispaced values of n, and in the s direction, we take 30 (again, this number has been calibrated) equispaced points or contour integrals. Thus, the total number of points or contour integrals to evaluate the residual in the example below is $4 \times 30 = 120$, instead of the 20,458 points that are present in the O-mesh, which leads to a significant CPU time saving when applying the GA.

Results shown in Sec. IV are calculated using (13), but we have checked that after postprocessing the snapshots, the residual (12) provides the same results, which emphasizes the robustness of the method. Without postprocessing, the residual (13) provides better results, since it is not affected by numerical errors in first-order derivatives. If these are avoided, both residuals are consistent with the governing equations; in fact, the residual (13) is closely related to the finite volume formulation of the CFD solver.

Once the POD amplitudes of the CFF have been calculated, we readily calculate both the SF using Eq. (5), with the same POD-mode

amplitudes of the CFF. This is because, as already explained in Sec. III.B.2, both the CFF and the SF coincide in the LER (Figs. 6 and 7). And also as in Sec. III.B.2, the jump across the shock wave is calculated as the difference between the CFF and SF in the TER (Figs. 6 and 7).

Three remarks are now noteworthy in connection with peculiarities of the method that differ from usual ROM calculations:

1) Both a reconstruction of the smooth field and the jump across the shock wave have been obtained simultaneously. Thus, the latter needs not be expanded into POD modes.

2) It is the Euler equations and not the original Navier–Stokes equations plus turbulence model that are used to calculate the residual. And the equations can still be applied either in their differential or conservative forms, even though the CFD simulations that provided the snapshots could be based on a different discretization. These facts make the method independent of the possible models of turbulence/numerical stabilizers that might have been used, which is convenient in industrial applications.

3) Only a small number of either points or contour integrals (about 120) are used to evaluate the residual that is minimized by the GA, which saves CPU time while preserving accuracy.

2. Calculation of the Shock Wave Trace and Internal Shape

Once the SF and the jump across the shock wave have been obtained, the position, trace, and internal shock wave shape remain to be calculated. To obtain these, the residual to be minimized by the GA is defined in terms of the right-hand sides of the conservation equations above as

$$H = \sum_{k} \sum_{i=1}^{4} \sqrt{|\text{EQ}_i(\Gamma_k)|}$$

where EQ_i denote the left-hand sides of the conservation Eqs. (10). The cycles (line integrals) have a rectangular shape in the curvilinear coordinates (s, n) and are centered on the previous guess of the shock wave position on the wall. The aspect ratio of the cycles and the number of cycles depend on the structure we are calculating. In all cases, cycles are contained in a region that extends vertically from the upper edge boundary of the boundary layer to a few lines below the boundary of the O-mesh, excluding both the boundary layer and a zone of localized CFD errors; horizontal extension coincides with the horizontal extension of the shock wave internal structure. Cycles to calculate each structure are as sketched in Fig. 8.

1) The position is calculated using only one cycle, which is as wide as possible within the above-mentioned region (see Fig. 8a).

2) The trace is calculated using as many cycles as possible, and these are selected to exhibit a height equal to one mesh interval and a width equal to the width of the SWR (see Fig. 8b).
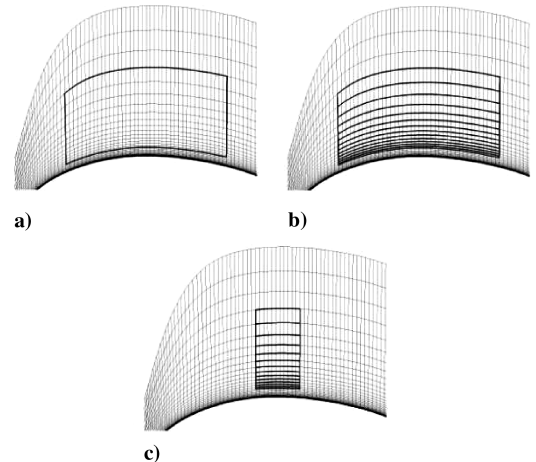

Fig. 8 Cycles used for evaluating the residual to calculate: a) position over the wall, b) the trace, and c) the internal shape.

3) The internal shape is calculated using the same cycles that provided the trace, except that their width is the same as that of the shock wave (see Fig. 8c).

3. Iteration to Obtain the ROM Solution

As described above, calculation of the complete solution involves four independent minimization processes, which are subsequently applied in an iterative way until the required accuracy is reached. Iteration is necessary because the various flow structures are coupled among each other. In other words, accuracy in the calculation of each structure leads to improvements in the approximation of the remaining structures. The four minimization processes are applied in the following order: 1) smooth field and shock wave jump, 2) shock wave position, 3) trace, 4) position, 5) internal shape, 6) position, 7) trace, and 8) position. Note that position is recalculated 3 times and the trace is recalculated twice in each iteration cycle. This is because these two structures show a large sensitivity on the parameters, and the available information to calculate them comes only from those snapshots that exhibit shock waves; the internal shape of the shock wave shows a smaller sensitivity on the parameters. The remaining shock wave structures are calculated using all available snapshots. Thus, calculation of the position and trace has shown to be crucial in the whole process. The process is repeated until differences between results in two consecutive cycles coincide within a specified relative error.

4. Genetic Algorithm

The genetic algorithm used to minimize the various residuals above is described elsewhere [17] and has been calibrated here to produce robust and reproducible results. In particular, the GA parameters on the various minimization processes above are as follows. Calculation of the CFF, the SF, and the shock wave structures (Sec. III.C.1 above) was made with the following GA parameters:

1) Ten thousand individuals are considered with a discretization of 10 bits per POD-mode amplitude of each individual.

2) Two percent of the elite individuals go straight into the next generation.

3) The crossover probability is equal to 0.8.

4) Five thousand bits are mutated in each generation.

5) The span allowed around the POD plus interpolation initial solution is equal to 50%.

6) The process is completed if the residual remains constant during 100 generations.

It is worth noting that the same GA parameters are appropriate to minimize the residuals (12) and (13), although the latter residual required less CPU time.

5. Required CPU Time

The method described above is much faster than the CFD solver, in spite of the use of a (slow) genetic algorithm minimization method and the fact that the software has not been optimized. For illustration, using a standard desktop PC (Pentium D 3.00 GHz, 1.87 GB RAM) in the test problem considered in this paper, the time needed to identify the shock wave structures (as explained in Sec. III.A) in the 117 snapshots is 4.6 CPU seconds per snapshot. Note that this step must be performed only once for each snapshot. The time cost of obtaining the POD modes for every structure and performing the various minimization processes ranges from 12 to 25 CPU minutes, depending on the required number of POD modes. Thus, this time compares well with the CFD computational cost (a minimum of 3 CPU hours).

IV. Results

The various parameters of the algorithm have been chosen (after some calibration) as follows:

1) The number of snapshots and the safety factor required in the method presented in Appendix A are $N_1 = 40$ and $F = 2.5$.

Table 1   Test points

Test	AOA	Mach number
PT11	−2.25	0.525
PT12	−1.25	0.525
PT13	1.25	0.525
PT14	2.25	0.525
PT21	−2.25	0.725
PT22	−1.25	0.725
PT23	1.25	0.725
PT24	2.25	0.725
PT31	−2.25	0.775
PT32	−1.25	0.775
PT33	1.25	0.775
PT34	2.25	0.775

2) The threshold used in Sec. III.A.1 to identify shock waves is $C'_{p0} = 9$.

3) The horizontal extension of the shock wave interval is $2L_1 = 12$ mesh points.

4) The semi-amplitude of the uncertainty in the shock wave position is $L_2 = 10$ mesh points (approximately, 5% of the chord).

5) The upper bound of the RMSE in POD is $\varepsilon = 10^{-3}$.

6) The upper bound of the RMSE used to choose the number of modes required is $\varepsilon = 10^{-3}$.

7) The RMSE bound to terminate the iterative process defined in Sec. III.C.3 is 10^{-3}.

To assess the behavior of the method, the aerodynamic coefficients (namely, the lift, drag, and moment coefficients) and the C_p distribution along the chord have been reconstructed in 12 test points, listed in Table 1; see also Fig. 9, in which the approximate boundary between the regions of existence/nonexistence of shock waves in the pressure and suction sides is also indicated. As is usually done in practical engineering situations, the test points were selected a priori, without all of the information on the existence of shock waves, and concentrated in the high Mach number region, where the strongest shock waves were expected.

As for the snapshots, we consider the following combinations:

1) Combination 1 consists of 117 (13×9) combined values of the following 13 values of the angle of attack −3, −2.5, −2, −1.5, −1, −0.5, 0, 0.5, 1, 1.5, 2, 2.5, and 3, and the following nine values of the Mach number 0.4, 0.45, 0.5, 0.55, 0.6, 0.65, 0.7, 0.75, and 0.8.

2) Combination 2 only contains the 63 (7×9) snapshots resulting from reducing in combination 1 the 13 cases on the angle of attack to the following seven equispaced values −3, −2, −1, 0, 1, 2, and 3.

3) Combination 3 only contains the 75 (13×5) snapshots resulting from reducing in combination 1 the nine cases on the
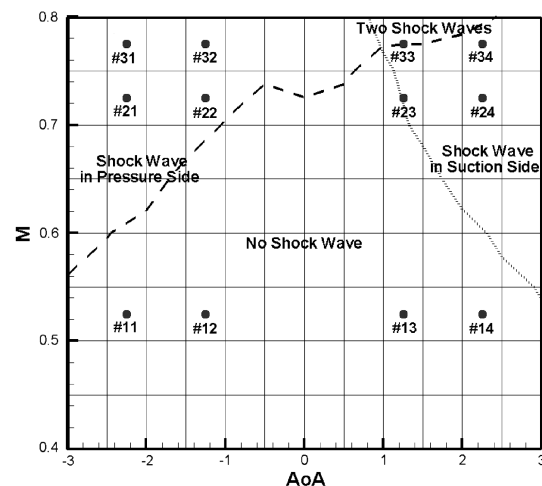

Fig. 9   Snapshots in combination 1 (the crossing points of the net) and test points (filled circles). The boundaries for the existence of shock waves are indicated with dashed and dotted lines, respectively.

Table 2   Lift, drag, and moment coefficients at the indicated test points, as calculated from CFD and our ROM, with combination 1; values smaller than 0.001 are rounded off to 0

Test point	$C_L/C_{L,\mathrm{ref}}$		$C_D/C_{D,\mathrm{ref}}$		$C_M/C_{M,\mathrm{ref}}$	
	CFD	POD plus GA	CFD	POD plus GA	CFD	POD plus GA
PT11	−1.094	−1.094	0.000	0.000	0.070	0.071
PT12	−0.800	−0.802	0.000	0.000	0.070	0.072
PT13	−0.069	−0.068	0.000	0.000	0.070	0.071
PT14	0.224	0.228	0.001	0.001	0.071	0.071
PT21	−1.476	−1.505	0.037	0.045	0.093	0.113
PT22	−1.117	−1.053	0.009	0.006	0.081	0.076
PT23	−0.094	−0.107	0.001	0.003	0.091	0.090
PT24	0.308	0.270	0.005	0.006	0.103	0.100
PT31	−1.212	−1.281	0.077	0.081	0.152	0.162
PT32	−1.117	−1.142	0.051	0.003	0.152	0.162
PT33	−0.117	−0.154	0.003	0.009	0.107	0.120
PT34	0.395	0.357	0.016	0.018	0.114	0.127

Mach number to the following five equispaced values 0.4, 0.5, 0.6, 0.7, and 0.8.

As a first result, Table 2 shows the global lift, drag, and moment coefficients of the airfoil, both as resulting from CFD and as calculated with our POD plus GA. Note that even the drag coefficient C_D is reasonably well calculated, in spite of the fact that POD plus GA relies on the Euler equations.

For completeness, several representative C_p distributions along the airfoil are plotted in Figs. 10–13, where a comparison with their CFD counterparts is also made. Figure 10 shows results at those test points that do not exhibit shock waves (see Fig. 9). Note that results are quite good with the three combinations and excellent (CFD and POD + GA plots are indistinguishable) with combinations 1 and 2, which indicates that information in the Mach number is less complete

than information in the angle of attack in combination 1. This conclusion will be confirmed in the remaining results below. Results in Fig. 10 also suggest that the number of snapshots taken at the low Mach number region can be reduced.

The remaining test points are considered in Fig. 12, where it is seen that results somewhat worsen at those test points that are close to either the lower boundary of existence of pressure-side shock waves (test point PT22) or the boundary of the parameter domain (test points PT31 and PT32).

The conclusion above (namely, that it is the shock wave in the pressure side that presents more difficulties in the present test problem) is further illustrated in Fig. 13, where two new test points at positive angle of attack are considered that are quite close to the existence boundary for the pressure-side shock wave. Note that using
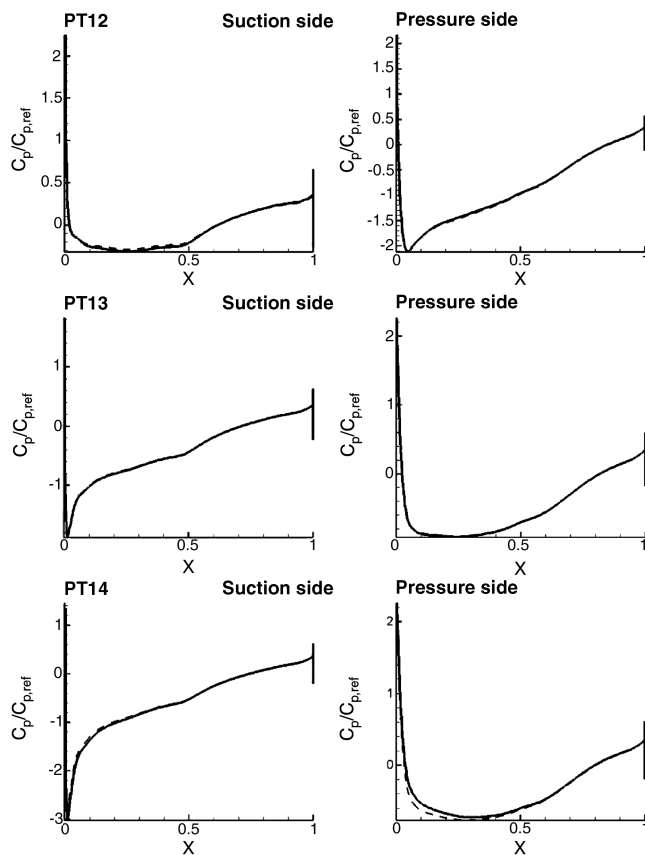

Fig. 10   Pressure coefficient distributions along the airfoil surface on test points PT11- PT14 as obtained using CFD (thick solid lines) and ROM, with combinations 1 (thin solid lines), 2 (dotted-dashed lines), and 3 (dashed lines).
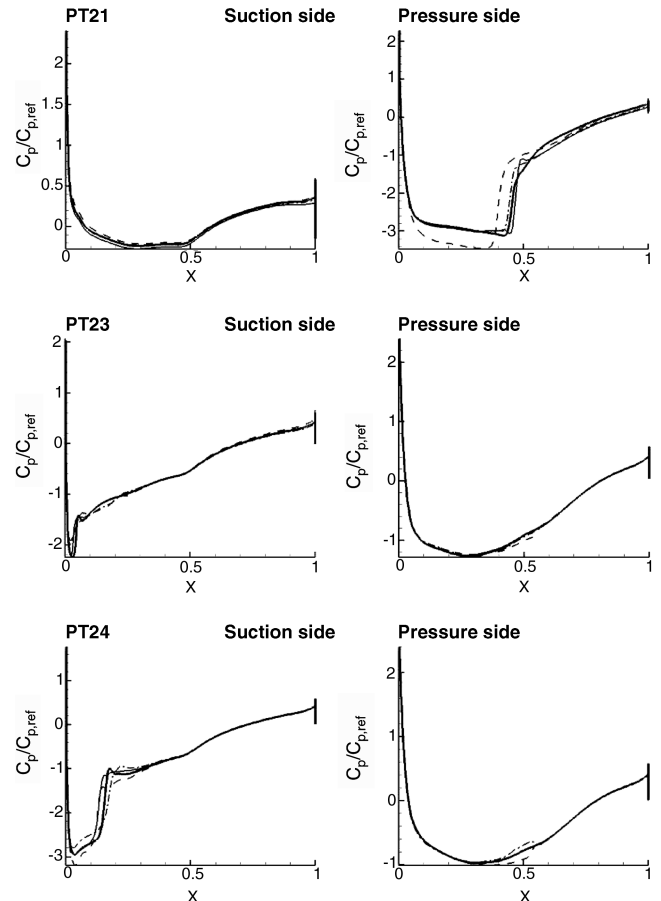

Fig. 11   Counterpart of Fig. 10 for the test points PT21, PT23, and PT24.
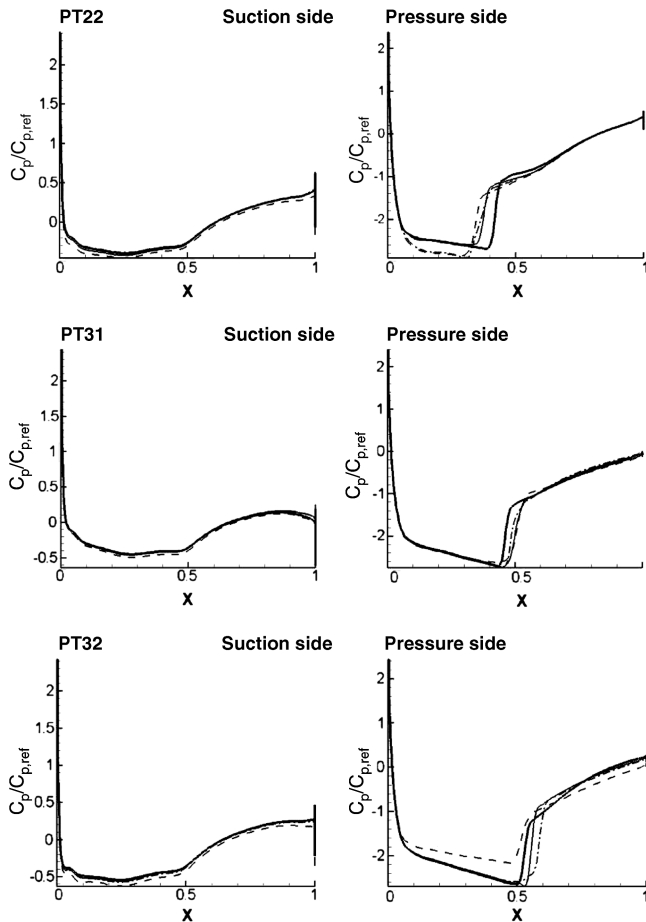
Fig. 12 Counterpart of Fig. 10 for the test points PT22, PT31, and PT32.

117 snapshots (combination 1), the method reasonably well approximates the suction-side shock wave, but then completely fails with the other shock wave.

These results would be highly improved if more snapshots were calculated in the problematic regions, which could be compensated
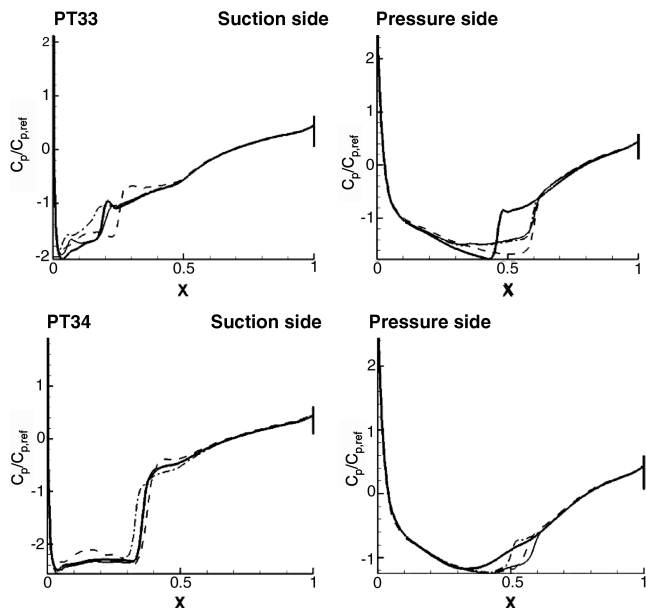

Fig. 13 Counterpart of Fig. 10 for two new test points: namely, test point PT33 at $(AOA, M) = (1.25, 7.75)$ and test point PT34 at $(AOA, M) = (2.25, 7.75)$.

saving snapshots at low Mach number, as indicated above. But this would require a method to select a priori the snapshots position in the parameter plane, which is not yet available. Such a method should take into account the peculiarities of the shock wave behavior.

Summarizing, results using all available snapshots (combination 1) are consistently better than whose using combinations 2 and 3, with fewer snapshots, even though the latter combinations produced reasonable results in various test points (in particular, when no shock wave is present). In fact, results were good except in the pressure-side shock wave existence/nonexistence boundary, which is understandable. Points near the boundary of the considered region instead do lead to difficulties. This could appear as counterintuitive at first sight, but note that we are not relying on interpolation (except to calculate the initial guess), but on projection of the governing equations on the POD modes plus a decomposition of the snapshots to extract the shock wave localized structures, which leads to difficulties near the shock wave existence/nonexistence interfaces; the fact that it is the pressure-side shock wave that posses the main difficulty is because this shock wave shows a richer structure in the parameter range we are considering. Thus, if the latter are well calculated (which seems to be the case if combination 1 is used), then results are reasonably good. No instability of the proposed ROM against higher modes truncation has been detected; in fact, retaining a few more modes than necessary produces essentially the same results. The ROM is robust against perturbations of the various calibration parameters, which have been chosen based on simple arguments. Unfortunately, checking the behavior of the ROM as the parameter range is increased was not possible, since the CFD algorithm shows unsteady behavior when either $M > 0.8$ or $|AOA| > 3°$.

V. Conclusions

A method has been presented to develop ROMs for transonic aerodynamic flows around a 2-D airfoil. The method is based on the following ingredients, which are new in this context (to our knowledge) and crucial to obtain computationally efficient ROMs:

1) Even though the snapshots were calculated using viscous equations, projection on the POD modes was made using the Euler equations, which makes the method independent of the peculiarities of the CFD method used to calculate the snapshots. This simplification gives good results and is based on the mathematical observation that the contribution of viscous terms in the projection formulas is negligible. This is because at these large values of the Reynolds numbers (on the order of 20 million), viscous effects are either small or concentrated in small regions of the computational domain (namely, boundary layers, shear layers, and shock waves).

2) Shock waves involve jumps in the flow variables, which present great difficulties in POD-based methods and require special treatment to avoid either a quite poor approximation or a huge number of snapshots. Such a treatment was presented in [18] to calculate transonic flows using a combination of PODlike methods and interpolation. The method has been extended here and combined with projection of the governing equations on the POD modes.

3) Projection on the POD manifold was made using only a subregion of the computational domain (a part of the small O-mesh around the airfoil in the test problem considered in this paper) and a small number of points in this subregion. As checked and further explained in [17], this simplification relies on some simple ideas and has been thoroughly used in the paper. For instance, projection to obtain the CFF and SF in Sec. III.C.1 was made using a subregion of the O-mesh (namely, the union of the LER and TER regions sketched in Fig. 7) after disregarding both the boundary layer and a vicinity of the upper boundary of the O-mesh, were CFD concentrated errors are present. Such a smaller subregion was selected to avoid shock waves, viscous effects, and concentrated CFD errors, and it provided a good approximation of the CFF (except near the shock waves, of course, which needed a different treatment). Thus, concentrating on smaller projection windows not only saves computational effort, but also makes the method much more flexible and allows avoiding CFD concentrated errors.

The method was applied to a specific test problem. Results were reasonably good (even in the boundary layer, where the neglected viscous effects are significant), except for parameter values in the shock wave existence/nonexistence boundary, where more snapshots would be needed. But in order to avoid the necessity of increasing the number of snapshots too much, fewer snapshots should be calculated in other regions of the parameter plane (small Mach number), where information was clearly redundant. Such a selection could have been done by hand, but we think that this is not a reasonable option, considering realistic industrial applications. Therefore, we are currently concentrating in developing a method to select snapshots in such a way that the CFD information required by the method is minimized.

The method can be extended to three-dimensional problems, provided that some a priori qualitative knowledge of the shock waves is at hand. For instance, in the test problem above, we can anticipate that no more than one shock wave exists in both the pressure and suction sides and that the shock wave trace can be written as $s = s_{sw}(n)$. Some similar a priori knowledge could also be anticipated in some parts of the aircraft such as the wings, the horizontal and vertical tail planes, and the fuselage. In these cases, the extension of the method developed in this paper also requires considering multiple shocks, since, e.g., wings may exhibit shock wave structures with more than one shock in certain chordwise sections; the extension of the ideas in the paper to multiple shocks is somewhat straightforward. Other parts like nacelles can exhibit shock wave traces with quite complex topology and need an even more flexible treatment, which is not a straightforward extension of the ideas in the paper and is the object of our current research.

Some of the ideas in the paper are also expected to be useful in treatment of nonsteady, transonic flows, but such an extension requires additional ingredients, even in the subsonic case. To our knowledge, ROMs of nonsteady aerodynamic flows have only be constructed (in, e.g., aeroelasticity [26]) to treat unsteady flows that are perturbations of steady ones. Efficient ROMs for fully nonlinear nonsteady flows could be made using ideas developed for simpler fluid dynamics problems [27,28], but these require first running the CFD solver along the whole unsteady solution to calculate the POD manifold, where the time-dependent governing equations are projected. Extension to aerodynamic flows of some new ideas (developed for simpler parabolic problems) based on the combined use of the CFD solver and a reduced Galerkin system [29] could give more efficient results. Again, this is the object of current research.

In any event, we expect that the results in the present paper will be a solid first step toward deriving ROMs for fully nonlinear transonic aerodynamics, which is a major open problem in the field.

Appendix A: Local Selection of the Snapshots to Calculate the Smooth Field

The idea in the algorithm below is to select those snapshots whose projection on an initial approximation of the solution is largest. For convenience, we perform the projection considering the SF instead of the CFF and use an inner product based on either the pressure- or suction-side region (see Fig. 6). The fact that selecting the snapshots with the SF to calculate the POD modes of the CFF gives good results is a further indication of the robustness of the method.

The algorithm to select the snapshots proceeds in four steps, as follows:

1) A first approximation of both the shock wave position and the SF is obtained via point-by-point interpolation of neighboring snapshots. The SWR is selected as explained in Sec. III.B.2.

2) If a shock wave is expected, then those snapshots that exhibit a shock wave outside the SWR are not used to calculate the POD manifold. If instead no shock wave is expected, only snapshots without a shock wave are considered.

3) We define a distance from each snapshot (labeled with the index j) to the SF obtained using POD plus interpolation. Such a distance D_j is defined as the orthogonal projection of the smooth field of the snapshot j, $(\rho u, \rho, p)_j^{SF}$, on the interpolated smooth field calculated above: namely,

$$D_j = \frac{\langle (\rho \tilde{u}, \tilde{\rho}, \tilde{p})^{SF}, (\rho u, \rho, p)_j^{SF} \rangle}{\sqrt{\langle (\rho \tilde{u}, \tilde{\rho}, \tilde{p})^{SF}, (\rho \tilde{u}, \tilde{\rho}, \tilde{p})^{SF} \rangle} \sqrt{\langle (\rho u, \rho, p)_j^{SF}, (\rho u, \rho, p)_j^{SF} \rangle}}$$

Here, the inner product is as defined in Eq. (4), but with the domain Ω equal to the whole suction or pressure region, defined in Sec. III.B.2. Using this distance, we calculate a covariance matrix considering the N_1 nearest snapshots, where N_1 is a number that is large enough to define the POD manifold; a value of N_1 on the order of the double of the expected POD manifold dimension is a good choice. Then a number of POD modes, $\tilde{N}_1$, is selected using the a priori error bound (2), to keep the RMSEs within a specified bound (which must be chosen after some calibration).

4) We define a safety factor $F > 1$ and retain the $N_2 = F\tilde{N}_1$ nearest snapshots to evaluate the POD manifold that will be finally used by the GA. It must be noted that N_2 can be either smaller or larger than N_1.

Appendix B: Recalculating the Wall-Normal Velocity Component by Means of the Continuity Equation

Here, we recalculate one of the velocity components of the POD modes in the CFF, either u or w (the one whose direction is closest to the normal to the airfoil), integrating the continuity equation: namely,

$$\frac{\partial(\rho u)}{\partial x} + \frac{\partial(\rho w)}{\partial z} = 0$$

with the remaining variables maintained at their original values.

The algorithm is somewhat standard and can be summarized as follows. First we note that because the flow is almost parallel in the O-mesh (near the airfoil), the estimate $|\rho w/(\rho u)| < 1$ applies except in a region near the leading edge, which is bounded by those points, in both the pressure and the suction sides, denoted as s_{limit}, where $|\rho w/(\rho u)| = 1$. Thus, the unknown to be calculated in this region is u, while it is w in the remaining part of the O-mesh. In each of these regions, we rewrite the continuity equation in (s, n) coordinates as

$$z_n \frac{\partial(\rho u)}{\partial s} - z_s \frac{\partial(\rho u)}{\partial n} - x_n \frac{\partial(\rho w)}{\partial s} + x_s \frac{\partial(\rho w)}{\partial n} = 0$$

where $x_s, x_n, z_s,$ and z_n are the derivatives of the physical coordinates, x and z, with respect to the curvilinear coordinates s and n. Note that this is a first-order equation in the n coordinate, which can be integrated taking as the initial condition at the first value of n ($n = 1$) the no slip boundary condition at the surface of the airfoil ($u = w = 0$) and marching in n with the following leapfrog scheme:

1) The s derivatives are discretized using centered differences in interior points and forward and backward derivatives at the upper and lower limit points, respectively; n derivatives instead are discretized using forward differences at $n = 1$ and using centered differences at $n > 1$.

2) According to such a discretization, marching in n is made with an implicit method at $n = 2$ and with an explicit method for $n > 2$. Note that we are not using forward differences here to march in n using an implicit scheme, because such a strategy would produce an error contamination from the lateral boundaries (namely, the extreme values of s) to the interior or the domain.

By construction, the resulting mass flux vector is not continuous at the extreme values of s. Thus, the mass flux must be smoothed, which is done in three steps, as follows:

1) A length L_3 is defined as the semi-amplitude of the interval in which we are going to smooth the mass flux vector. After some calibration, we take $L_3 = 2.5\%$ of the chord (e.g., five nodes in the example presented in Sec. IV).

2) Two intervals are defined, $[s_{limit} - L_3, s_{limit}]$ and $[s_{limit}, s_{limit} + L_3]$, which will be used to smooth the horizontal and vertical mass fluxes, respectively.

3) The complete field is overlapped with the new field integrated above using the following formula:

$$(\rho u)^{\text{corrected}}(s, n) = \varphi(s)(\rho u)^{\text{CFF}}(s, n)$$
$$+ (1 - \varphi(s))(\rho u)^{\text{integrated}}(s, n)$$
$$(\rho w)^{\text{corrected}}(s, n) = \varphi(s)(\rho w)^{\text{integrated}}(s, n)$$
$$+ (1 - \varphi(s))(\rho w)^{\text{CFF}}(s, n) \qquad (B1)$$

where $\varphi(s)$ is the sigmoidal function defined in (2), except for the term $s_w + t(n) - L_1$, which is substituted by $s_{\text{limit}} \mp L_3$ (the $-$ and $+$ signs corresponding to the horizontal and vertical mass fluxes, respectively).

Acknowledgments

References

[1] Barone, M. F., Kalashnikova, I., Segalman, D. J., and Thornquist, H. K., "Stable Galerkin Reduced Order Models for Linearized Compressible Flow," *Journal of Computational Physics*, Vol. 228, 2009, pp. 1932–1946.
doi:10.1016/j.jcp.2008.11.015

[2] Bui-Thanh, T., Willcox, K., Ghattas, O., and van Bloemen Waanders, B., "Goal Oriented, Model-Constrained Optimization for Reduction of Large-Scale Systems," *Journal of Computational Physics*, Vol. 224, 2007, pp. 880–896.
doi:10.1016/j.jcp.2006.10.026

[3] Willcow, K., and Peraire, J., "Balanced Model Reduction via the Proper Orthogonal Decomposition," *AIAA Journal*, Vol. 40, 2002, pp. 2323–2330.
doi:10.2514/2.1570

[4] Rowley, C. W., "Model Reduction for Fluids Using Balanced Proper Orthogonal Decomposition," *International Journal of Bifurcation and Chaos in Applied Sciences and Engineering*, Vol. 15, No. 3, 2005, pp. 997–1013.
doi:10.1142/S0218127405012429

[5] Prajna, S., "POD Model Reduction with Stability Guarantee," *Proceedings of the 42nd IEEE Conference on Decision and Control*, Vol. 5, IEEE Press, Piscataway, NJ, Dec. 2003, pp. 5254–5258.

[6] Barrault, M., Maday, Y., Cuong, N., and Patera, A. T., "An 'Empirical Interpolation' Method: Application to Efficient Reduced-Basis Discretization of Partial Differential Equations," *Comptes Rendus. Mathématique*, Vol. 339, 2004, pp. 667–672.
doi:10.1016/j.crma.2004.08.006

[7] Ali, S., Damodaran, M., and Willcox, K., "Approximate Low Dimensional Models Based on Proper Orthogonal Decomposition for Black-Box Applications," *Singapore-MIT Alliance Symposium*, Singapore, 23–24 Jan. 2007.

[8] Hollkamp, J. J., and Gordon, R. W., "Reduced-Order Models for Nonlinear Response Prediction: Implicit Condensation and Expansion," *Journal of Sound and Vibration*, Vol. 318, 2008, pp. 1139–1153.
doi:10.1016/j.jsv.2008.04.035

[9] Bai, Z., Dewilde, P. M., and Freund, R. W., "Reduced-Order Modeling," *Handbook of Numerical Analysis, Volume XIII. Special Volume: Numerical Methods in Electromagnetics*, edited by W. H. A. Schilders, and E. J. W. ter Maten, Elsevier, New York, 2005, pp. 825–895.

[10] LeGresley, P. A., and Alonso, J. J., "Investigation of Nonlinear Projection for POD Based Reduced Order Models for Aerodynamics," AIAA Paper 2001-0926, 2001, pp. 1–15.

[11] Lieu, T., Farhat, C., and Lesoinne, M., "Reduced-Order Fluid/Structure Modeling of a Complete Aircraft Configuration," *Computer Methods in Applied Mechanics and Engineering*, Vol. 195, 2006, pp. 5730–5742.
doi:10.1016/j.cma.2005.08.026

[12] Iemma, U., and Gennaretti, M., "Reduced-Order Modeling for Linearized Aeroelasticity of Fixed Wings in Transonic Flight," *Journal of Fluids and Structures*, Vol. 21, 2005, pp. 243–255.
doi:10.1016/j.jfluidstructs.2005.05.014

[13] Thomas, J. P., Dowell, E. H., and Hall, K. C., "Static/Dynamic Correction Approach for Reduced-Order Modeling of Unsteady Aerodynamics," *Journal of Aircraft*, Vol. 43, No. 4, 2006, pp. 865–878.
doi:10.2514/1.12349

[14] Allen, C. B., Taylor, N. V., Fenwick, C. L., Gaitonde, A. L., and Jones, D. P., "A Comparison of Full Nonlinear and Reduced Order Aerodynamic Models in Control Law Design Using a Two-Dimensional Aerofoil Model," *International Journal of Numerical Methods in Engineering*, Vol. 64, 2005, pp. 1628–1648.
doi:10.1002/nme.1421

[15] Lucia, D. J., Beran, P. S., and Silva, W. A., "Reduced-Order Modeling: New Approaches for Computational Physics," *Progress in Aerospace Sciences*, Vol. 40, 2004, pp. 51–117.
doi:10.1016/j.paerosci.2003.12.001

[16] Alonso, D., Velazquez, A., and Vega, J. M., "Robust Reduced Order Modeling of Heat Transfer in a Back Step Flow," *International Journal of Heat and Mass Transfer*, Vol. 52, 2009, pp. 1149–1157.
doi:10.1016/j.ijheatmasstransfer.2008.09.011

[17] Alonso, D., Velazquez, A., and Vega, J. M., "A Method to Generate Computationally Efficient Reduced Order Models," *Computer Methods in Applied Mechanics and Engineering*, Vol. 198, 2009, pp. 2683–2691.
doi:10.1016/j.cma.2009.03.012

[18] Lorente, L. S., Vega, J. M., and Velazquez, A., "Generation of Aerodynamics Databases Using High-Order Singular Value Decomposition," *Journal of Aircraft*, Vol. 45, 2008, pp. 1779–1788.
doi:10.2514/1.35258

[19] Sirovich, L., "Turbulence and the Dynamics of Coherent Structures," *Quarterly of Applied Mathematics*, Vol. 45, 1987, pp. 561–590.

[20] Schwamborn, D., Gerhold, T., and Heinrich, R., "The DLR TAU-Code: Recent Applications in Research and Industry," *European Conference on Computational Fluid Dynamics, ECCOMAS CFD 2006*, Sept. 2006.

[21] Brodersen, O., Eisfeld, B., Raddatz, J., and Frohnapfel, P., "DLR Results from the Third AIAA CFD Drag Prediction Workshop," 45th AIAA Aerospace Sciences Meeting and Exhibit, Reno, NV, AIAA Paper 2007-259, Jan. 2007.

[22] Edwards, J. R., and Chandra, S., "Comparison of Eddy Viscosity Transport Turbulence Models for Three Dimensional, Shock Separated Flowfields," *AIAA Journal*, Vol. 34, No. 4, 1996, pp. 756–763.
doi:10.2514/3.13137

[23] Liepmann, H. W., and Roshko, A., *Elements of Gasdynamics*, Wiley, New York, 1957.

[24] Fletcher, R., *Practical Methods of Optimization*, Wiley, New York, 1987.

[25] Akima, H., "A Method of Bivariate Interpolation and Smooth Surface Fitting for Irregular Distributed Data Points," *ACM Transactions on Mathematical Software*, Vol. 4, 1978, pp. 148–164.
doi:10.1145/355780.355786

[26] Dowell, E. H., and Hall, K. C., "Modeling of Fluid-Structure Interaction," *Annual Review of Fluid Mechanics*, Vol. 33, 2001, pp. 445–490.
doi:10.1146/annurev.fluid.33.1.445

[27] Sirisup, S., Karniadakis, G. E., Xiu, D., and Kevrekidis, I. G., "Equations-Free/Galerkin-Free POD Assisted Computation of Incompressible Flows," *Journal of Computational Physics*, Vol. 207, 2005, pp. 568–587.
doi:10.1016/j.jcp.2005.01.024

[28] Couplet, M., Basdevant, C., and Sagaut, P., "Calibrated Reduced-Order Pod-Galerkin System for Fluid Flow Modelling," *Journal of Computational Physics*, Vol. 207, 2005, pp. 192–220.
doi:10.1016/j.jcp.2005.01.008

[29] Rapun, M. L., and Vega, J. M., "Reduced Order Models Based on Local POD Plus Galerkin Projection," *Journal of Computational Physics*, Vol. 229, 2010, pp. 3046–3063.
doi:10.1016/j.jcp.2009.12.029

K. Willcox
Associate Editor